PAPER

Check for updates

Modulating the microenvironment of AuPd nanoparticles using metal–organic frameworks for selective methane oxidation†

Jianfei Sui,‡[a] Ming-Liang Gao,‡[a] Chengyuan Liu,[b] Yang Pan, [ID][b] Zheng Meng, [ID]*[a] Daqiang Yuan [ID][c] and Hai-Long Jiang [ID]*[a]

Direct and selective oxidation of methane (CH_4) into methanol (CH_3OH) under ambient conditions remains a grand challenge because of the high energy barrier of CH_4 activation and the complicated processes involved. Herein, by incorporating AuPd alloy nanoparticles (NPs) into a series of Cu^{2+}-doped metal–organic frameworks (MOFs), namely AuPd@Cu-UiO-66$_x$, efficient and direct catalytic conversion of CH_4 to CH_3OH can be achieved at mild temperature (70 °C) with H_2O_2 as an oxidant. The Cu-UiO-66 serving as the microenvironment parameter not only regulates the electronic state of AuPd NPs to improve the CH_4 adsorption and activation, but also affects the generation of hydroxyl radicals ($^{\cdot}OH$) in H_2O_2 reaction pathways, which consequently results in a volcano-type dependency of the CH_3OH selectivity on the Cu contents. This work represents the first finding on achieving direct catalytic oxidation of CH_4 to CH_3OH under mild conditions by modulating the microenvironment of catalytic centers based on a MOF platform.

Introduction

The direct conversion of methane, the major component of natural gas, to olefins, aromatics, oxygenates, and other products, has been recognized as a potentially economical and environmentally friendly way to generate value-added chemicals from abundant and inexpensive sources.[1–3] Among various routes of methane conversion, the direct and selective oxidation of methane to methanol, known as the 'Holy Grail' reaction in catalysis science,[4,5] is particularly promising. However, this transformation has long been challenged by the stable and inert C–H bonds (ΔH_{C-H} = 104 kcal mol^{-1}), low polarizability, and negligible electron affinity of methane.[4–8] Therefore, energy-intensive routes are conventionally required for CH_4 activation.[2,3] In addition, the challenges in the CH_4 to CH_3OH process are also tangled by the fact that CH_3OH can be more easily oxidized than CH_4, which leads to unexpected peroxidation products.[6,7] Therefore, the development of suitable systems for

efficient and selective direct conversion of CH_4 to CH_3OH under mild conditions is highly desirable yet challenging.

To achieve selective oxidation of CH_4 to CH_3OH under mild conditions, environmentally benign hydrogen peroxide (H_2O_2) has been adopted as the oxidant.[4,6,9–11] Unfortunately, this may lead to the formation of methyl-hydroperoxide (CH_3OOH) as the main product by the combination of $^{\cdot}CH_3$ with dissolved O_2 originating from the decomposition of H_2O_2,[9,12] or produce a significant amount of byproducts due to the overoxidation of methanol by $^{\cdot}OH$ originating from the homocleavage of H_2O_2.[10,11] Although a few systems, including metal-modified zeolites and metal nanoparticle-based heterostructures,[5,11–14] have been employed, the rational control of the catalytic performance is still far from satisfactory to achieve both high selectivity and activity. The above situation is likely rooted in the complex and highly interconnected processes involved in catalytic CH_4 oxidation using H_2O_2, such as the activation of CH_4 and H_2O_2, the degradation of H_2O_2, overoxidation of methanol, and more.[15–17] Evidently, the complicated nature of the H_2O_2-participated CH_4 oxidation requires a precise balance of these processes for achieving high activity and selectivity. A platform that allows the sophisticated control of H_2O_2 homocleavage by microenvironment modulation is thus highly desirable.

Based on the above analysis, it is assumed that metal–organic frameworks (MOFs), a class of porous crystalline materials featuring high surface areas and tailorable structures,[17–20] would be an ideal platform for creating a suitable microenvironment for hosted active centers. Different components involved in catalytic sites and the microenvironment can work

[a]Hefei National Laboratory for Physical Sciences at the Microscale, Department of Chemistry, University of Science and Technology of China, Hefei, Anhui 230026, P. R. China. E-mail: zhengmeng@ustc.edu.cn; jianglab@ustc.edu.cn

[b]National Synchrotron Radiation Laboratory (NSRL), University of Science and Technology of China, Hefei, Anhui 230029, P. R. China

[c]State Key Laboratory of Structural Chemistry, Fujian Institute of Research on the Structure of Matter, Chinese Academy of Sciences, Fuzhou 350002, P. R. China

† Electronic supplementary information (ESI) available: Materials and instrumentation, experimental section, and supplemental figures and tables. See DOI: https://doi.org/10.1039/d3ta03712f

‡ These authors contributed equally to this work.

This journal is © The Royal Society of Chemistry 2023

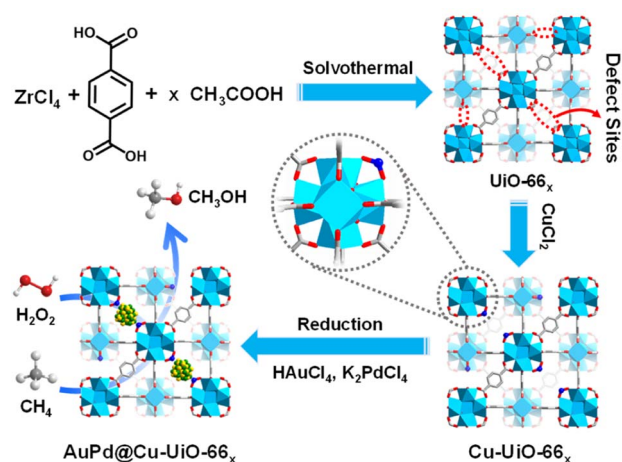*J. Mater. Chem. A*, 2023, 11, 18733–18739 | 18733

Fig. 1 Schematic illustration showing the synthetic process for AuPd@Cu-UiO-66$_x$.

synergistically to target optimal catalytic performance. Specifically, the permanent porosity of MOFs can provide congenital advantages for stabilizing active metal nanoparticles (NPs).[21–25] The high tailorability of MOFs makes it feasible to introduce extra auxiliary components through various modification strategies, enabling the microenvironment modulation for metal NPs in a rational manner.[19]

In this work, the representative MOF, UiO-66 with defects in varying degrees, denoted as UiO-66$_x$ (x represents the molar ratio of (acetic acid)/(the linker), x = 0, 50, 100, 150, and 200), has been fabricated. Upon furnishing Cu^{2+} onto the defect sites of Zr-oxo clusters of UiO-66, AuPd NPs are further incorporated to afford AuPd@Cu-UiO-66$_x$ composite (Fig. 1). AuPd NPs were utilized in our study for their capability in partial methane oxidation.[11] Remarkably, anchoring Cu species to the Zr-oxo clusters around AuPd NPs effectively tunes the selectivity to CH$_3$OH with a volcano-type dependency on the Cu loadings, where the optimized CH$_3$OH selectivity is as high as 80.97%. The regulated selectivity arises from the combined effect of the enhanced CH$_4$ adsorption and the weakened ·OH formation accompanied by the Cu^{2+} anchoring. Although MOFs have been reported in the quasi-catalytic CH$_4$ oxidation under high-temperature in the gas phase,[26,27] this study, integrating AuPd active sites and the microenvironment modulation by systematically tailoring Cu loadings based on a MOF platform, achieves highly selective CH$_4$ oxidation under mild conditions.

Results and discussion

UiO-66$_x$ compounds with different amounts of structural defects were synthesized by reacting ZrCl$_4$ and terephthalic acid with different equivalents of acetic acid as a modulator in DMF. Powder X-ray diffraction (XRD) patterns suggest that all UiO-66$_x$ compounds maintain similar high crystallinity to UiO-66 (Fig. S1†). Scanning electron microscopy (SEM) images display that the sizes of MOF particles gradually increase and the morphology changes from intergrown prototypes to octahedral nanocrystals, along with more acetic acid being used (Fig. S2†).

N$_2$ sorption isotherms demonstrate that the Brunauer–Emmett–Teller (BET) area for UiO-66$_x$ gradually increases from 736 to 1151 m^2 g^{-1} while the pore volume increases from 0.55 to 0.67 cm^3 g^{-1} with increased amounts of acetic acid (Fig. S3†). Cu-UiO-66$_x$ were prepared by a microwave-assisted reaction of CuCl$_2$·2H$_2$O and UiO-66$_x$ in acetonitrile. Inductively coupled plasma atomic emission spectrometry (ICP-AES) analysis demonstrates that the Cu loadings are approximately 0.41–2.42 wt% in Cu-UiO-66$_x$ (Table S1†). To identify the existing form of Cu and its electronic state in the catalysts, Cu-UiO-66$_{200}$ is chosen considering that its higher Cu content than other catalysts would be beneficial to the characterization precision. The diffuse reflectance infrared Fourier transform (DRIFT) spectra show that the intensities of peaks at 3673 and 2769 cm^{-1}, respectively attributed to the terminal –OH/–OH$_2$ and μ$_3$-OH on the defect sites, are significantly lower in Cu-UiO-66$_{200}$ than those in UiO-66, which supports the immobilization of Cu atoms to the chelating/defect sites in Cu-UiO-66$_x$ (Fig. S4†).[28–30] The Raman spectrum for Cu-UiO-66$_{200}$ clearly showed the Cu–O vibration peak at 150 cm^{-1}, which also supports that Cu is anchored to UiO-66 (Fig. S5†).[31] The Cu K-edge X-ray absorption near-edge structure (XANES) spectrum of Cu-UiO-66$_{200}$ displays an absorption threshold analogous to that of CuO, indicating that the oxidation state of Cu is about +2 (Fig. 2a). The Fourier-
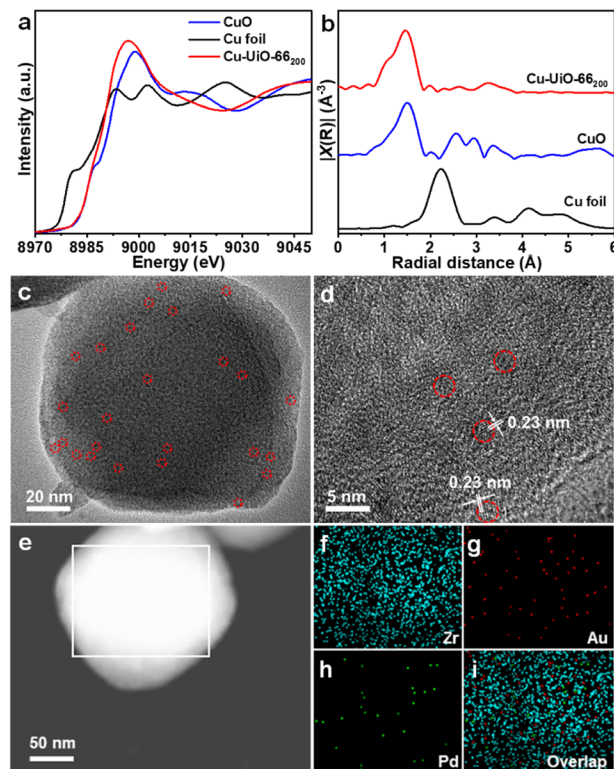

Fig. 2 (a) The normalized XANES spectra, (b) FT-EXAFS spectra for Cu-UiO-66$_{200}$, CuO, and Cu foil. (c) TEM and (d) HRTEM images of AuPd@Cu-UiO-66$_{100}$. (e–i) High-angle annular darkfield scanning transmission electron microscopy image of AuPd@Cu-UiO-66$_{100}$, and the corresponding Zr, Au, Pd, and overlapped elemental mapping for the selected area.

transformed extended X-ray absorption fine structure (FT-EXAFS) spectrum of Cu-UiO-66$_{200}$ shows only one dominant peak at approximately 1.5 Å, confirming the atomically dispersed Cu sites in Cu-UiO-66$_{200}$ (Fig. 2b).[30]

To prepare AuPd@Cu-UiO-66$_x$, the mixture of HAuCl$_4$ and K$_2$PdCl$_4$ aqueous solution was impregnated into Cu-UiO-66$_x$ and subsequently reduced in a H$_2$/Ar atmosphere at 200 °C. Powder XRD patterns suggest that the crystallinity of Cu-UiO-66$_x$ is maintained after the incorporation of AuPd NPs (Fig. S6†). In addition, the comparison shows that the (200), (220), and (222) diffraction peaks of HKUST-1 were absent in AuPd@Cu-UiO$_x$, indicating that there is no formation of HKUST-1 in our work when Cu is added to the MOF and subjected to high temperature (Fig. S6†). The contents of Au and Pd determined by ICP-AES are similar across all AuPd@Cu-UiO-66$_x$ samples, which are approximately 3.5 wt% for Au and 1.5 wt% for Pd, respectively (Table S1†). The octahedral shape of UiO-66$_x$ remained after the AuPd incorporation, as demonstrated by the SEM images and the selected area electron diffraction (SAED) pattern has been obtained to demonstrate that UiO-66 is stable under the tested condition (Fig. S7†). In addition, transmission electron microscopy (TEM) observation of AuPd@Cu-UiO-66$_x$ shows that the tiny AuPd NPs with rough sizes of 1.5 nm, matching the pore sizes of defective UiO-66,[32,33] are highly dispersed throughout Cu-UiO-66$_x$ particles (Fig. 2c, S8–S12†). Although the sizes of the AuPd NPs can be larger than the free volume of the octahedron cages (12 Å) in UiO-66, we hypothesize that large-sized NPs may penetrate multiple adjacent cages through the pore aperture or appear where the defects are present. The direct comparison between the high-angle annular dark-field scanning transmission electron microscopy (HAADF-STEM) and secondary electron STEM (SE-STEM) images acquired at the same location supports that the AuPd NPs are located inside the crystallites of AuPd@Cu-UiO-66$_{100}$ (Fig. S13†).[34–36] Lattice fringes with a *d*-spacing of ~0.23 nm are observed by high-resolution TEM (HRTEM) (Fig. 2d), consistent with the (111) plane of AuPd NPs.[37] The energy-dispersive X-ray mapping results suggest homogeneous distributions of Au and Pd elements in the MOF particle (Fig. 2e–i), further supporting the well-dispersed feature of AuPd NPs in UiO-66$_x$. N$_2$ sorption isotherms demonstrate that the porous structures of Cu-UiO-66$_x$ are all maintained after the incorporation of AuPd NPs, albeit with slightly decreased BET areas due to the mass and pore occupation by AuPd NPs (Fig. S14†). The pore size distributions of the AuPd@Cu-UiO-66$_x$ are mostly in the range of 7–15 Å, which are still large enough for CH$_4$, H$_2$O$_2$, and intermediates involved in CH$_4$ oxidation.

The performance of AuPd@Cu-UiO-66$_x$ catalysts for direct catalytic oxidation of CH$_4$ to CH$_3$OH has been evaluated in an aqueous H$_2$O$_2$ solution (Fig. 3 and Tables S2, S3†). Without the incorporation of AuPd NPs, UiO-66 or Cu-UiO-66 alone fails to catalyze the oxidation of CH$_4$. The Au@UiO-66 shows good reactivity for CH$_4$ oxidation to give the oxygenated products CH$_3$OH, CH$_3$OOH, and HCOOH, among which CH$_3$OH only takes up a very small portion with a selectivity of 30.19%. Although Pd@UiO-66 shows a moderately high CH$_3$OH selectivity of 50.39%, its reactivity toward CH$_4$ oxidation is very poor since the total oxygenated products are only 39% of those for
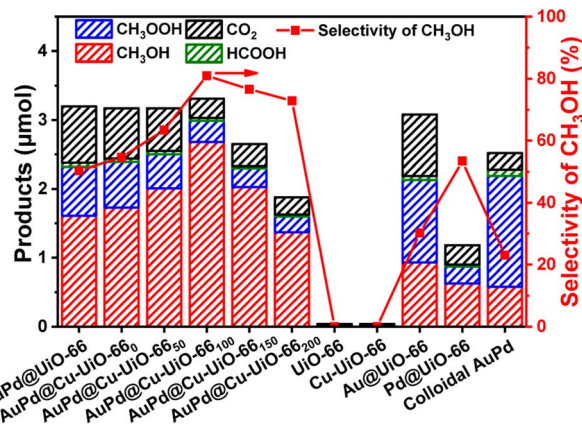

Fig. 3 Catalytic performance of AuPd@UiO-66, AuPd@Cu-UiO-66$_x$, UiO-66, Cu-UiO-66, Au@UiO-66, Pd@UiO-66, and colloidal AuPd NPs in the CH$_4$ oxidation (reaction conditions: catalyst 27 mg, CH$_4$ pressure 30 bar, H$_2$O$_2$ 0.5 M (aq), 70 °C, reaction time 30 min).

Au@UiO-66. In contrast to these comparison catalysts, AuPd@UiO-66 gives a reasonable CH$_3$OH selectivity of 53.84% and a much higher CH$_3$OH yield (1.61 μmol) than both Au@UiO-66 (0.93 μmol) and Pd@UiO-66 (0.63 μmol), suggesting AuPd NPs are indispensable for high activity and selectivity in the conversion. Despite this, colloidal AuPd NPs present a low CH$_3$OH selectivity of 23% while CH$_3$OOH is the major species (64%) among all the oxidation products. The significantly lower CH$_3$OH yield of colloidal AuPd NPs (0.58 μmol) than that of AuPd@UiO-66 (1.61 μmol) indicates the critical role of the MOF in this reaction.

Upon introducing Cu species into AuPd@UiO-66, an enhanced CH$_3$OH selectivity of 54.57% is observed with AuPd@Cu-UiO-66$_0$ as the catalyst. With increased Cu loading, the selectivity to CH$_3$OH first exhibits a trend of increase and reaches a maximum of 80.97% with a normalized production rate of 198.52 μmol g$_{cat}^{-1}$ h^{-1} using AuPd@Cu-UiO-66$_{100}$. Further increasing the Cu content leads to a decrease of the selectivity to 76.60% and 72.87% for AuPd@Cu-UiO-66$_{150}$ and AuPd@Cu-UiO–66$_{200}$, respectively. The selectivity of CH$_3$OH exhibits a volcano-type dependency on the Cu loadings in AuPd@Cu-UiO-66$_x$ (Fig. 3), unambiguously demonstrating that the Cu species effectively regulates the AuPd selectivity in the partial oxidation of CH$_4$ to CH$_3$OH. The comprehensive normalized conversions for all the C1 products have also been provided (Table S2†). It is worth noting that by simply increasing the Cu content from 0.4 wt% in AuPd@Cu-UiO-66$_0$ to 1.4 wt% in AuPd@Cu-UiO-66$_{100}$, a 48% improvement of the methanol selectivity can be achieved. Since Cu in AuPd@Cu-UiO-66$_x$ is anchored to the defect sites of UiO-66, the defect sites exposed in AuPd@Cu-UiO-66$_x$ catalysts will be negligible. Therefore, with other chemical parameters kept the same in AuPd@Cu-UiO-66$_x$, the observed difference of the selectivity provided by AuPd@Cu-UiO-66$_x$ should be ascribed to their different Cu loadings. Considering that Cu actually accounts for only very small mass percentages in the catalysts, the dependency of selectivity on Cu loading highlights the importance of the precise control of the microenvironment to the optimization of catalytic performance. In addition, a recent

This journal is © The Royal Society of Chemistry 2023

J. Mater. Chem. A, 2023, **11**, 18733–18739 | **18735**

report on the use of AuPd NPs encapsulated by ZIF-8 gave a selectivity of 21.9% for CH_3OH.[38] Compared with AuPd@Cu-UiO-66$_{100}$, the sharp performance contrast is another sign of the significance of the microenvironment modulation.

To examine the source of the products, the isotope trace experiment by using $^{13}CH_4$ has been conducted. Synchrotron radiation photoionization mass spectrometry (SR-PIMS) for the reaction mixture gives peaks at $m/z = 33$ and $m/z = 47$ at a photon energy of 11.8 eV, which are respectively corresponding to $^{13}CH_3OH$ and $H^{13}COOH$ (Fig. 4a). The results unambiguously confirm that CH_4 is the exclusive carbon source of CH_3OH and HCOOH products, which also demonstrate the successful implementation of catalytic CH_4 oxidation over the AuPd@Cu-UiO-66$_{100}$ catalyst. Interestingly, a peak at $m/z = 31$ assigned to $H^{13}CHO$ is also observed (Fig. 4a). HCHO has been confirmed as the primary and active intermediate in the oxidation of CH_3OH.[39,40] However, the low concentration of HCHO in the reaction and the overlap of its chemical shift with solvent make its detection extremely challenging. In our system, the signal of HCHO becomes more apparent when CH_3OH is adopted as the reactant (Fig. S15†). The *in situ* SR-PIMS test demonstrates the appearance of HCHO after 10 min in the CH_3OH oxidation, prior to the observation of HCOOH (Fig. S16†). HCOOH can be detected when HCHO is used as the reactant (Fig. S17†). These results support that CH_4 is first converted to the desired product CH_3OH, and further overoxidized into HCOOH through the formation of intermediate HCHO (Fig. 4b).

N_2 sorption isotherms (Fig. S18†) and powder XRD pattern of AuPd@Cu-UiO-66$_{100}$ after catalysis manifest that the porosity and crystalline feature of the MOF is maintained (Fig. S19†). No identifiable peak assigned to AuPd NPs can be observed in powder XRD pattern, reflecting that AuPd NPs are not agglomerated during the catalysis, in line with the TEM observation (Fig. S20†). The metal loadings are maintained after the reaction based on ICP-AES results, suggesting the absence of metal leaching during the reaction (Table S4†). The FT-IR, ^{1}H NMR spectra, and elemental analysis of AuPd@Cu-UiO-66$_{100}$ before and after the reaction are nearly identical, implying that the organic components in the catalysts keep intact during the reaction (Fig. S21, S22, and Table S4†). Furthermore, no apparent activity and selectivity loss occur to AuPd@Cu-UiO-66$_{100}$ in three consecutive cycles (Fig. S23†), demonstrating its good reusability. All the above results evidence the stability of the catalysts under the tested conditions.
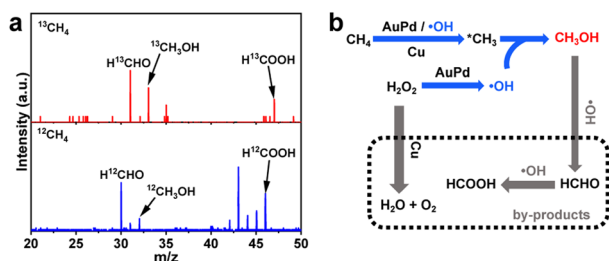

Fig. 4 (a) Photoionization mass spectrum of the products using $^{13}CH_4$ and $^{12}CH_4$ as the reactant. (b) Proposed reaction path for methane oxidation over AuPd@UiO-66$_{100}$.

To disclose the role of Cu in catalysis, X-ray photoelectron spectroscopy (XPS) has been conducted to investigate the oxidation state of Au and Pd species (Fig. S24†). The AuPd@UiO-66 presents two sets of peaks: one set of peaks are at binding energies of 83.65 and 87.35 eV, corresponding to Au^0 $4f_{7/2}$ and Au^0 $4f_{5/2}$, respectively; the other set of peaks at 335.22 and 340.61 eV are ascribed to $3d_{5/2}$ and $3d_{3/2}$ of Pd^0, respectively.[41–45] Compared to monometallic Au^0 and Pd^0, both Au 4f and Pd 3d peaks in AuPd@UiO-66 shift to lower binding energies. The electronic state change of Au and Pd indicates the formation of AuPd alloy, which is supported by the previous reports.[37,41–45] With increased Cu loadings, the Au 4f and Pd 3d peaks gradually shift to higher binding energies in AuPd@Cu-UiO-66$_x$. These changes may be ascribed to the electron-withdrawing effect of Cu^{2+}, leading to electron transfer from AuPd to Cu^{2+}.[29] To further probe the modulated electronic state of AuPd NPs in AuPd@Cu-UiO-66$_x$, the carbon monoxide (CO) adsorption analysis using diffuse reflectance infrared Fourier transform spectroscopy (DRIFTS) has been carried out (Fig. S25†). Both adsorption bands of linearly adsorbed CO on Au (2150–2000 cm^{-1}) and twofold bridge-bonded CO on Pd (2000–1900 cm^{-1}) shift to higher wavenumbers with the change of wavenumber >20 cm^{-1} when creasing Cu loadings, which further supports enhanced electron transfer from AuPd to the MOFs with increased Cu loadings.[46,47] This phenomenon can be ascribed to the electron-withdrawing effect of Cu^{2+} attached to the Zr-oxo clusters of UiO-66, leading to the electron transfer from Au and Pd to Cu. With the increase of Cu content, the electron-withdrawing effect becomes stronger, resulting in a gradual increase of the binding energy. Taking all these spectroscopic results together, it is suggested that the Cu^{2+} incorporation effectively modulates the AuPd electronic state, which may be responsible for the observed different CH_3OH selectivity of AuPd@Cu-UiO-66$_x$.[14,48]

It is generally believed that CH_4 oxidation using H_2O_2 as an oxidant involves at least three key steps, the adsorption and activation of CH_4 to form active $*CH_x$ species on the surface of catalysts[13] or through the attack of CH_4 by $\cdot OH$,[49] the homolytic cleavage of H_2O_2 to generate $\cdot OH$, and the combination of $*CH_x$ and $\cdot OH$ (Fig. 4b).[5] To investigate the adsorption of CH_4 on catalysts, CH_4 temperature-programmed desorption coupled with mass spectrometric analysis (TPD-MS) has been carried out. The results show that the desorption temperature of CH_4 from AuPd@Cu-UiO-66$_{100}$ is approximately 184 °C, in comparison to 158 °C for AuPd@UiO-66 (Fig. 5a, S26†), revealing stronger CH_4 adsorption on AuPd@Cu-UiO-66$_{100}$. The CH_4 sorption displays the higher CH_4 adsorption capacity (17.6 cm^3 g^{-1}) of AuPd@Cu-UiO-66$_{100}$ than AuPd@UiO-66 (13.5 cm^3 g^{-1}) at 1 bar and 298 K (Fig. S27†). From AuPd@UiO-66 to AuPd@Cu-UiO-66$_{100}$, the increase of CH_4 adsorption is 30%, which is higher than the magnitude of the increase of the BET area, supporting the enhanced CH_4 adsorption of the latter. This enhanced CH_4 adsorption would be beneficial to its activation on AuPd sites and competition with the CH_3OH adsorption to avoid over-oxidation,[50] giving rise to enhanced activity and selectivity toward CH_3OH.

To identify the possible behavior of CH_4 after its adsorption, near-ambient pressure XPS (NAP-XPS) has been conducted.
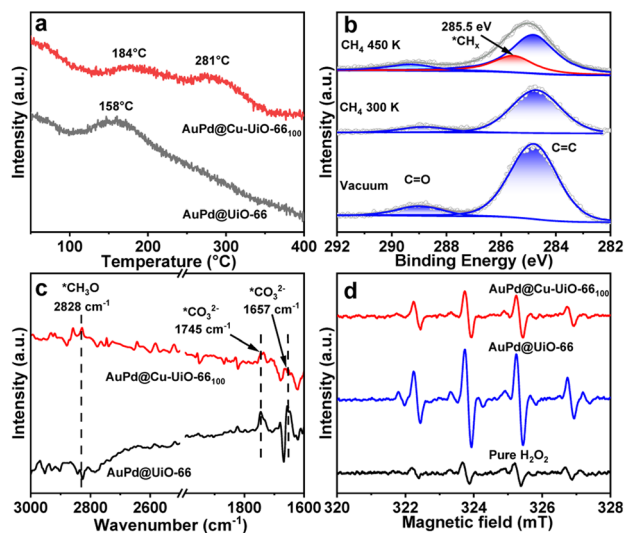
Fig. 5 (a) TPD-MS profiles ($m/z = 15$) of CH_4 on AuPd@UiO-66 and AuPd@UiO-66$_{100}$. (b) The C 1s XPS spectra of the AuPd@UiO-66$_{100}$ in ultrahigh vacuum and after introducing 1 mbar of CH_4 at different temperatures. (c) DRIFT spectra of CH_4 adsorbed AuPd@UiO-66 and AuPd@UiO-66$_{100}$ after being purged with Ar gas for 30 min. (d) EPR trapping experiment over AuPd@UiO-66 and AuPd@UiO-66$_{100}$ with H_2O_2 as the oxidant and DMPO as the radical trapping agent.

Before CH_4 exposure, the C 1s spectrum of AuPd@Cu-UiO-66$_{100}$ displays two peaks at 284.8 and 288.8 eV attributed to the C=C, C–C, C–H, and C=O bonds in the MOF linkers (Fig. 5b).[51,52] The subsequent exposure of the sample to 1 mbar of CH_4 at 300 K doesn't result in additional peaks, probably due to the overlap of signals between CH_4 and C=C, C–C, and C–H bonds of the MOF. When the temperature is raised to 450 K, deconvolution of the C 1s spectrum gives a new peak at 285.5 eV (Fig. 5b). This peak can be assigned to the $*CH_x$ species, which may include CH_3, CH_2, and CH, inferring the activation of CH_4 on the catalyst.[50] *In situ* DRIFTS has been further conducted to investigate the transformation of CH_x species on different catalyst surfaces in the presence of H_2O_2. When CH_4 is exposed to the catalyst for 30 minutes, peaks at 1305 and 3015 cm^{-1} assigned to the typical vibration of absorbed CH_4 are observed (Fig. S28†).[53,54] After the physically adsorbed CH_4 is removed by flushing Ar flow through an H_2O_2 aqueous solution, the peaks in the ranges of 1500–1800 cm^{-1} and 2700–3000 cm^{-1} appear (Fig. 5c). The peaks at 1657 and 1745 are assigned to $*CO_3^{2-}$, and the signal at 2828 cm^{-1} is ascribed to the $*CH_3O$ intermediate.[53–55] The appearance of these peaks indicates the transformation of $*CH_x$ to oxygen-containing species on the catalyst with the participation of H_2O_2. Compared to those in AuPd@UiO-66, the intensity of the peak at 2828 cm^{-1} ($*CH_3O$) increases and the intensities at 1657 and 1745 cm^{-1} ($*CO_3^{2-}$) decrease in the presence of AuPd@Cu-UiO-66$_{100}$, in line with its enhanced CH_3OH selectivity. The above results demonstrate that AuPd NPs play several important roles in the reaction, in which they not only affect CH_4 adsorption but also influence the activation and transformation of CH_4. The modulated electronic state of AuPd

by the incorporated Cu^{2+} will, thus, have a profound effect on the CH_3OH selectivity.

Reactive oxygen species originating from H_2O_2, such as superoxide anion radicals ($O_2^{\cdot-}$) and hydroxyl radicals ($^{\cdot}OH$), are the other group of important intermediates in CH_4 oxidation by H_2O_2. Electron paramagnetic resonance (EPR) experiments have been conducted to detect the radical species involved in the reaction. With 5,5-dimethyl-pyrroline-*N*-oxide (DMPO) as a radical trapping agent, EPR spectra exhibit a characteristic signal of DMPO-OH (Fig. 5d). This result suggests that $^{\cdot}OH$ is the main active species in methane oxidation. Compared with AuPd@Cu-UiO-66, the intensity of EPR signals in AuPd@Cu-UiO-66$_{100}$ is lower, indicating its reduced generation of $^{\cdot}OH$. No DMPO-CH$_3$ peak is observed likely attributed to the fast combination of as-generated $^{\cdot}CH_3$ with the relatively abundant $^{\cdot}OH$.[56,57] When CH_4 is replaced by CH_3OH, products HCOOH and CO_2 are detected (Fig. S29†), implying that $^{\cdot}OH$ generated from H_2O_2 also participates in the overoxidation process. Generally, H_2O_2 has two competitive pathways in CH_4 oxidation, the generation of O_2 and H_2O through decomposition and the formation of $^{\cdot}OH$ from homolytic cleavage.[15,46–49] It is found that the decomposition rate of H_2O_2 increases with increased Cu content in AuPd@Cu-UiO-66$_x$ (Fig. S30†), probably owing to the catalytic effect of Cu in H_2O_2 decomposition through the Cu^I/Cu^{II} redox couple.[16] Therefore, with increased Cu loadings in AuPd@Cu-UiO-66$_x$, the generation of $^{\cdot}OH$ will be more or less suppressed due to the enhanced decomposition of H_2O_2. The introduction of Cu at too low loadings will result in the formation of excess $^{\cdot}OH$ and lead to overoxidation during CH_4 oxidation. On the other hand, a too-high loading of Cu^{2+} will reduce the concentration of $^{\cdot}OH$ around the catalytic sites, leading to inhibition of oxidation. Therefore, only a suitable content of Cu^{2+} will allow optimal catalytic performance.[58]

The above-mentioned characterization studies and *in situ* technique shed light on the mechanism of the oxidation of CH_4 to CH_3OH mediated by anchored Cu regarding the activation of CH_4 and the formation of CH_3OH as shown in Fig. 4b, in which the Cu species plays multiple roles as the microenvironment factors for AuPd sites. Firstly, the incorporation of Cu modulates the AuPd electronic state, giving rise to enhanced adsorption of CH_4 on AuPd NPs. Secondly, the presence of Cu regulates H_2O_2 reaction pathways. With increased Cu loadings, the generation of $^{\cdot}OH$ is reduced, which weakens both the CH_3OH formation and its overoxidation processes.

Conclusions

In summary, AuPd alloy NPs incorporated into Cu-modified MOF, namely AuPd@Cu-UiO-66$_x$, have been fabricated and exhibit excellent activity and selectivity in the direct oxidation of CH_4 to CH_3OH in aqueous solution with H_2O_2 as an oxidant under mild conditions. The selectivity presents a volcano-type trend with increased Cu amount in the catalysts, among which AuPd@Cu-UiO-66$_{100}$, featuring an optimized Cu^{2+} content, possesses the best CH_3OH selectivity of 80.97%. A slight change of Cu content from 0.4 wt% in AuPd@UiO-66$_0$ to 1.4 wt% in AuPd@UiO-66$_{100}$ significantly boosts the CH_3OH

This journal is © The Royal Society of Chemistry 2023

J. Mater. Chem. A, 2023, **11**, 18733–18739 | **18737**

selectivity by 48%. Mechanistic investigations reveal that the auxiliary Cu^{2+} on the MOF skeleton, acting as the microenvironment, has a profound influence on AuPd NPs for CH_4 oxidation, where it not only modulates the AuPd electronic state to improve CH_4 adsorption but also regulates the formation of $^{\cdot}OH$ in H_2O_2 reaction pathways. This work provides significant insights into the intricate processes involved in CH_4 oxidation toward optimized methanol selectivity, which would open an avenue to microenvironment modulation of active sites for enhanced catalysis.

Author contributions

H.-L. J. conceived the idea and supervised the project. J. S. and M.-L. G. performed the experiments and collected the data. C. L. and Y. P. conducted the synchrotron radiation photoionization mass spectrometry experiments. D. Y. conducted the CH_4 sorption isotherm experiments. H.-L. J., Z. M., and J. S. co-wrote the manuscript. All authors discussed the results and commented on the manuscript.

Conflicts of interest

There are no conflicts to declare.

Acknowledgements

References

1 P. Schwach, X. Pan and X. Bao, *Chem. Rev.*, 2017, **117**, 8497–8520.

2 P. Tang, Q. Zhu, Z. Wu and D. Ma, *Energy Environ. Sci.*, 2014, **7**, 2580–2591.

3 D. Saha, H. A. Grappe, A. Chakraborty and G. Orkoulas, *Chem. Rev.*, 2016, **116**, 11436–11499.

4 P. Tomkins, M. Ranocchiari and J. A. van Bokhoven, *Acc. Chem. Res.*, 2017, **50**, 418–425.

5 Z. Jin, L. Wang, E. Zuidema, K. Mondal, M. Zhang, J. Zhang, C. Wang, X. Meng, H. Yang, C. Mesters and F. S. Xiao, *Science*, 2020, **367**, 193–197.

6 X. Meng, X. Cui, N. P. Rajan, L. Yu, D. Deng and X. Bao, *Chem*, 2019, **5**, 2296–2325.

7 Z. Liu, E. Huang, I. Orozco, W. Liao, R. M. Palomino, N. Rui, T. Duchon, S. Nemsak, D. C. Grinter, M. Mahapatra, P. Liu, J. A. Rodriguez and S. D. Senanayake, *Science*, 2020, **368**, 513–517.

8 Y. Zhou, L. Zhang and W. Wang, *Nat. Commun.*, 2019, **10**, 506.

9 M. Ravi, V. L. Sushkevich, A. J. Knorpp, M. A. Newton, D. Palagin, A. B. Pinar, M. Ranocchiari and J. A. van Bokhoven, *Nat. Catal.*, 2019, **2**, 485–494.

10 C. Hammond, M. M. Forde, M. H. Ab Rahim, A. Thetford, Q. He, R. L. Jenkins, N. Dimitratos, J. A. Lopez-Sanchez, N. F. Dummer, D. M. Murphy, A. F. Carley, S. H. Taylor, D. J. Willock, E. E. Stangland, J. Kang, H. Hagen, C. J. Kiely and G. J. Hutchings, *Angew. Chem., Int. Ed.*, 2012, **51**, 5129–5133.

11 S. J. Freakley, N. Dimitratos, D. J. Willock, S. H. Taylor, C. J. Kiely and G. J. Hutchings, *Acc. Chem. Res.*, 2021, **54**, 2614–2623.

12 N. Agarwal, S. J. Freakley, R. U. McVicker, S. M. Althahban, N. Dimitratos, Q. He, D. J. Morgan, R. L. Jenkins, D. J. Willock, S. H. Taylor, C. J. Kiely and G. J. Hutchings, *Science*, 2017, **358**, 223–227.

13 S. Bai, Y. Xu, P. Wang, Q. Shao and X. Huang, *ACS Catal.*, 2019, **9**, 6938–6944.

14 C. Williams, J. H. Carter, N. F. Dummer, Y. K. Chow, D. J. Morgan, S. Yacob, P. Serna, D. J. Willock, R. J. Meyer, S. H. Taylor and G. J. Hutchings, *ACS Catal.*, 2018, **8**, 2567–2576.

15 Y. Xing, Z. Yao, W. Li, W. Wu, X. Lu, J. Tian, Z. Li, H. Hu and M. Wu, *Angew. Chem., Int. Ed.*, 2021, **60**, 8889–8895.

16 R. Serra-Maia, F. M. Michel, Y. Kang and E. A. Stach, *ACS Catal.*, 2020, **10**, 5115–5123.

17 H. C. Zhou and S. Kitagawa, *Chem. Soc. Rev.*, 2014, **43**, 5415–5418.

18 B. Li, H. M. Wen, Y. Cui, W. Zhou, G. Qian and B. Chen, *Adv. Mater.*, 2016, **28**, 8819–8860.

19 L. Jiao, J. Wang and H.-L. Jiang, *Acc. Mater. Res.*, 2021, **2**, 327–339.

20 L. Z. Dong, L. Zhang, J. Liu, Q. Huang, M. Lu, W. X. Ji and Y. Q. Lan, *Angew. Chem., Int. Ed.*, 2020, **59**, 2659–2663.

21 A. Aijaz, A. Karkamkar, Y. J. Choi, N. Tsumori, E. Ronnebro, T. Autrey, H. Shioyama and Q. Xu, *J. Am. Chem. Soc.*, 2012, **134**, 13926–13929.

22 X. Li, T. W. Goh, L. Li, C. Xiao, Z. Guo, X. C. Zeng and W. Huang, *ACS Catal.*, 2016, **6**, 3461–3468.

23 Q. Yang, Q. Xu and H.-L. Jiang, *Chem. Soc. Rev.*, 2017, **46**, 4774–4808.

24 F. Chen, K. Shen, J. Chen, X. Yang, J. Cui and Y. Li, *ACS Cent. Sci.*, 2019, **5**, 176–185.

25 D. Chen, W. Yang, L. Jiao, L. Li, S. H. Yu and H.-L. Jiang, *Adv. Mater.*, 2020, **32**, e2000041.

26 J. Baek, B. Rungtaweevoranit, X. Pei, M. Park, S. C. Fakra, Y. S. Liu, R. Matheu, S. A. Alshmimri, S. Alshehri, C. A. Trickett, G. A. Somorjai and O. M. Yaghi, *J. Am. Chem. Soc.*, 2018, **140**, 18208–18216.

27 J. Zheng, J. Ye, M. A. Ortuno, J. L. Fulton, O. Y. Gutierrez, D. M. Camaioni, R. K. Motkuri, Z. Li, T. E. Webber, B. L. Mehdi, N. D. Browning, R. L. Penn, O. K. Farha, J. T. Hupp, D. G. Truhlar, C. J. Cramer and J. A. Lercher, *J. Am. Chem. Soc.*, 2019, **141**, 9292–9304.

28 J. Sui, H. Liu, S. Hu, K. Sun, G. Wan, H. Zhou, X. Zheng and H.-L. Jiang, *Adv. Mater.*, 2022, **34**, e2109203.

18738 | *J. Mater. Chem. A*, 2023, **11**, 18733–18739

This journal is © The Royal Society of Chemistry 2023

29 C. Xu, Y. Pan, G. Wan, H. Liu, L. Wang, H. Zhou, S. H. Yu and H.-L. Jiang, *J. Am. Chem. Soc.*, 2019, **141**, 19110–19117.

30 A. M. Abdel-Mageed, B. Rungtaweevoranit, M. Parlinska-Wojtan, X. Pei, O. M. Yaghi and R. J. Behm, *J. Am. Chem. Soc.*, 2019, **141**, 5201–5210.

31 Y. Deng, A. D. Handoko, Y. Du, S. Xi and B. S. Yeo, *ACS Catal.*, 2016, **6**, 2473–2481.

32 Y. Jiao, Y. Liu, G. Zhu, J. T. Hungerford, S. Bhattacharyya, R. P. Lively, D. S. Sholl and K. S. Walton, *J. Phys. Chem. C*, 2017, **121**, 23471–23479.

33 F. Ahmadijokani, R. Mohammadkhani, S. Ahmadipouya, A. Shokrgozar, M. Rezakazemi, H. Molavi, T. M. Aminabhavi and M. Arjmand, *Chem. Eng. J.*, 2020, **399**, 125346.

34 P. Wang, B. Wang, Y. Liu, L. Li, H. Zhao, Y. Chen, J. Li, S. F. Liu and K. Zhao, *Angew. Chem., Int. Ed.*, 2020, **59**, 23100–23106.

35 L. Lin, J. Liu, X. Liu, Z. Gao, N. Rui, S. Yao, F. Zhang, M. Wang, C. Liu, L. Han, F. Yang, S. Zhang, X. D. Wen, S. D. Senanayake, Y. Wu, X. Li, J. A. Rodriguez and D. Ma, *Nat. Commun.*, 2021, **12**, 6978.

36 H. Wang, X. Liu, W. Yang, G. Mao, Z. Meng, Z. Wu and H.-L. Jiang, *J. Am. Chem. Soc.*, 2022, **144**, 22008–22017.

37 J. Long, H. Liu, S. Wu, S. Liao and Y. Li, *ACS Catal.*, 2013, **3**, 647–654.

38 G. Xu, A. Yu, Y. Xu and C. Sun, *Catal. Commun.*, 2021, **158**, 106338.

39 W. Wen, S. Yu, C. Zhou, H. Ma, Z. Zhou, C. Cao, J. Yang, M. Xu, F. Qi, G. Zhang and Y. Pan, *Angew. Chem., Int. Ed.*, 2020, **59**, 4873–4878.

40 Y. Liu, F. M. Kirchberger, S. Muller, M. Eder, M. Tonigold, M. Sanchez-Sanchez and J. A. Lercher, *Nat. Commun.*, 2019, **10**, 1462.

41 J. Xu, T. White, P. Li, C. He, J. Yu, W. Yuan and Y. F. Han, *J. Am. Chem. Soc.*, 2010, **132**, 10398–10406.

42 X. Zhu, Q. Guo, Y. Sun, S. Chen, J. Q. Wang, M. Wu, W. Fu, Y. Tang, X. Duan, D. Chen and Y. Wan, *Nat. Commun.*, 2019, **10**, 1428.

43 W. Guan, Y. Zhang, C. Yan, Y. Chen, Y. Wei, Y. Cao, F. Wang and P. Huo, *ChemSusChem*, 2022, **15**, e202201041.

44 W. Zhan, Q. He, X. Liu, Y. Guo, Y. Wang, L. Wang, Y. Guo, A. Y. Borisevich, J. Zhang, G. Lu and S. Dai, *J. Am. Chem. Soc.*, 2016, **138**, 16130–16139.

45 Y. Qiu, L. Xin, Y. Li, I. T. McCrum, F. Guo, T. Ma, Y. Ren, Q. Liu, L. Zhou, S. Gu, M. J. Janik and W. Li, *J. Am. Chem. Soc.*, 2018, **140**, 16580–16588.

46 N. E. Kolli, L. Delannoy and C. Louis, *J. Catal.*, 2013, **297**, 79–92.

47 E. K. Gibson, A. M. Beale, C. R. A. Catlow, A. Chutia, D. Gianolio, A. Gould, A. Kroner, K. M. H. Mohammed, M. Perdjon, S. M. Rogers and P. P. Wells, *Chem. Mater.*, 2015, **27**, 3714–3720.

48 M. H. Ab Rahim, R. D. Armstrong, C. Hammond, N. Dimitratos, S. J. Freakley, M. M. Forde, D. J. Morgan, G. Lalev, R. L. Jenkins, J. A. Lopez-Sanchez, S. H. Taylor and G. J. Hutchings, *Catal. Sci. Technol.*, 2016, **6**, 3410–3418.

49 R. Serra-Maia, F. M. Michel, T. A. Douglas, Y. Kang and E. A. Stach, *ACS Catal.*, 2021, **11**, 2837–2845.

50 Y. Fan, W. Zhou, X. Qiu, H. Li, Y. Jiang, Z. Sun, D. Han, L. Niu and Z. Tang, *Nat. Sustain.*, 2021, **4**, 509–515.

51 H. Prats, R. A. Gutierrez, J. J. Pinero, F. Vines, S. T. Bromley, P. J. Ramirez, J. A. Rodriguez and F. Illas, *J. Am. Chem. Soc.*, 2019, **141**, 5303–5313.

52 Z. Liu, P. Lustemberg, R. A. Gutierrez, J. J. Carey, R. M. Palomino, M. Vorokhta, D. C. Grinter, P. J. Ramirez, V. Matolin, M. Nolan, M. V. Ganduglia-Pirovano, S. D. Senanayake and J. A. Rodriguez, *Angew. Chem., Int. Ed.*, 2017, **56**, 13041–13046.

53 X. Chen, Y. Li, X. Pan, D. Cortie, X. Huang and Z. Yi, *Nat. Commun.*, 2016, **7**, 12273.

54 H. Song, X. Meng, S. Wang, W. Zhou, S. Song, T. Kako and J. Ye, *ACS Catal.*, 2020, **10**, 14318–14326.

55 Q.-L. Zhu and Q. Xu, *Chem*, 2016, **1**, 220–245.

56 X. Cui, H. Li, Y. Wang, Y. Hu, L. Hua, H. Li, X. Han, Q. Liu, F. Yang, L. He, X. Chen, Q. Li, J. Xiao, D. Deng and X. Bao, *Chem*, 2018, **4**, 1902–1910.

57 W. Zhao, Y. Shi, Y. Jiang, X. Zhang, C. Long, P. An, Y. Zhu, S. Shao, Z. Yan, G. Li and Z. Tang, *Angew. Chem., Int. Ed.*, 2021, **60**, 5811–5815.

58 A. Barnes, R. J. Lewis, D. J. Morgan, T. E. Davies and G. J. Hutchings, *Catalysts*, 2022, **12**, 1396.

This journal is © The Royal Society of Chemistry 2023

J. Mater. Chem. A, 2023, **11**, 18733–18739 | **18739**